The Electrochemical Society
Advancing solid state & electrochemical science & technology

Effect of Applying a Carbon Coating on the Crystal Structure and De-/Lithiation Mechanism of Mn-Doped ZnO Lithium-Ion Anodes

View the article online for updates and enhancements.

The Electrochemical Society
Advancing solid state & electrochemical science & technology

240th ECS Meeting ORLANDO, FL

Orange County Convention Center Oct 10-14, 2021

Abstract submission deadline extended: April 23rd

SUBMIT NOW

Effect of Applying a Carbon Coating on the Crystal Structure and De-/Lithiation Mechanism of Mn-Doped ZnO Lithium-Ion Anodes

Tobias Eisenmann,[1,2] Adele Birrozzi,[1,2] Angelo Mullaliu,[1,2] Gabriele Giuli,[3]
Angela Trapananti,[3] Stefano Passerini,[1,2,*] and Dominic Bresser[1,2,**,z]

[1]*Helmholtz Institute Ulm (HIU), 89081 Ulm, Germany*
[2]*Karlsruhe Institute of Technology (KIT), 76021 Karlsruhe, Germany*
[3]*School of Science and Technology, University of Camerino, 62032 Camerino, Italy*

The introduction of transition metal dopants such as Fe and Co in zinc oxide enables substantially enhanced reversible capacities and greater reversibility of the de-/lithiation reactions occurring. Herein, we report a comprehensive analysis of the electrochemical processes taking place in Mn-doped ZnO ($Zn_{0.9}Mn_{0.1}O$) and carbon-coated $Zn_{0.9}Mn_{0.1}O$ upon de-/lithiation. The results shed light on the impact of the dopant chemistry and, especially, its coordination in the crystal structure. When manganese does not replace zinc in the wurtzite structure, only a moderate improvement in electrochemical performance is observed. However, when applying the carbonaceous coating, a partial reduction of manganese and its reallocation in the crystal structure occur, leading to a substantial improvement in the material's specific capacity. These results provide important insights into the impact of the lattice position of transition metal dopants—a field that has received very little, essentially no attention, so far.

Supplementary material for this article is available online

The energy requests from portable electronics in the past years and, more recently, the electrification of modern transportation are driving the continuous improvement of lithium-ion batteries (LIBs),[1–3] in spite of the fact that they already offer substantially higher energy and power densities than other battery technologies.[1,2] An important role in this regard plays the use of graphite as the state-of-the-art active material for the negative electrode due to its high theoretical specific capacity of 372 mAh g^{-1} and its low de-/lithiation potential, allowing for very high energy densities at the full-cell level.[3] However, the demand for increasingly faster charging rates, especially in the automotive sector, has led to vast research efforts in identifying alternative active material candidates for the negative electrode, including different Li$^+$ storage mechanisms such as conversion and alloying.[4–12] Conversion-type materials like, e.g., transition metal oxides offer higher specific capacities than graphite. Nevertheless, the average de-/lithiation potential is relatively high, which negatively affects the achievable energy density in full-cells. Moreover, they commonly suffer from a rather large voltage hysteresis, which impacts the energy efficiency.[10] Alloying materials, such as Si, Ge, or Sn, for instance, offer even higher specific capacities (up to 3578 mAh g^{-1} for Si) at lower de-/lithiation potentials. This high lithium uptake, however, is accompanied by extensive volume changes and rapid structural degradation of the materials and electrodes.[6,13]

Furthermore, alloying-metal oxides such as ZnO and SnO$_2$ have been reported as negative electrode material candidates. They offer decent theoretical specific capacities (ZnO: 988 mAh g^{-1}, SnO$_2$: 1494 mAh g^{-1}) when assuming a reversible Li$_2$O formation (at elevated potentials); the latter compound also serving as a buffering matrix to accommodate the volume variation.[14–16] Nonetheless, the Li$_2$O formation is essentially irreversible, limiting the eventual specific capacity to 329 mAh g^{-1} (ZnO) and 782 mAh g^{-1} (SnO$_2$), i.e., the alloying reaction only.[17] This drawback can be overcome by doping the metal oxide with non-alloying transition metals, which renders the Li$_2$O formation reversible and, thus, leads to substantially higher capacities.[18–22] The choice of the transition metal, however, has been shown to have a great impact on the electrochemical behavior in the

case of SnO$_2$. Among Mn, Co, and Fe as dopants, the former provides the highest theoretical specific energy due to its lower redox potential compared to the others,[23] while a combination with Co enables further enhanced performance.[24] Following pre-lithiation of the anode active material, a full-cell composed of carbon-coated $Sn_{0.9}Co_{0.05}Mn_{0.05}O_2$ (SCMO-C) and high-voltage $LiNi_{0.5}Mn_{0.5}O_4$ (LNMO) as the active material for the negative and positive electrode, respectively, provided a specific energy of 312 Wh kg^{-1} (based on the mass of the two active materials; cycled at 1 C; with 1 C = 147 mA g$^{-1}_{LNMO}$), which is slightly higher than what has been reported for lab-scale graphite||LNMO cells with about 300 Wh kg^{-1} at C/3 (1 C = 147 mA g$^{-1}_{LNMO}$).[25] Somewhat lower values have been very recently reported for $Zn_{0.9}Fe_{0.1}O$-C||LNMO cells with around 160 to 280 Wh kg^{-1} at 1 C (1 C = 147 mA g$^{-1}_{LNMO}$), revealing a substantial impact of the degree of pre-lithiation on the achievable specific energy[26]; in fact, not only on the specific energy, but also the energy efficiency.[26,27] With regard to the effect of introducing manganese into ZnO, however, there has been only one study reporting the electrochemical performance of such material, to the best of our knowledge —which was rather poor with a rapid capacity fading to about 210 mAh g^{-1} before stabilizing.[28]

In this study, we report a fundamental investigation of the impact of introducing manganese as dopant in ZnO by means of an in-depth *ex situ/operando* structural and electrochemical characterization. We show that the incorporation of manganese leads to substantially higher capacities—in particular when combined with a carbon coating. Moreover, we emphasize the key role of the carbon coating, which is far more important than anticipated. In fact, the coating process results in the partial reduction and reorganization of manganese in the crystal structure, which significantly contributes to the enhanced reversibility of the de-/lithiation reaction.

Experimental

Material synthesis.—$Zn_{0.9}Mn_{0.1}O$ was synthesized following a previously reported procedure.[20] Stoichiometric amounts of zinc (II) gluconate (Alfa Aesar) and manganese (II) acetate tetrahydrate (ACROS ORGANICS) were dissolved in ultra-pure water with a total ion concentration of 0.2 M. This solution was added to a solution comprising 1.2 M sucrose. After stirring for 15 min, the temperature was increased to 160 °C to evaporate the water. Subsequently, the temperature was risen to 300 °C to initiate sucrose

decomposition until a solid, foam-like resin was obtained. This resin was ground and calcined for 3 h at 400 °C (alternatively also at 360 °C, 450 °C, and 500 °C) in a muffle furnace with a heating rate of 3 K min^{-1} (Nabertherm). Pure ZnO was synthesized without adding the Mn precursor.

For the application of the carbon coating, $Zn_{0.9}Mn_{0.1}O$ and sucrose were dispersed in ultrapure water in a weight ratio of 10:9. A planetary ball mill (Fritsch Vario-Planetary Mill Pulverisette 4), operated at 400/−800 rpm for 3 h (1.5 h in each direction), was used to homogenize the dispersion. After drying the sample at 80 °C overnight, the solid powder was manually ground and calcined at 500 °C for 4 h in a tubular furnace (Nabertherm) with a heating rate of 3 K min^{-1} under a constant argon flow.

Physicochemical characterization.—Scanning electron microscopy (SEM) was performed using a Zeiss Crossbeam 340 field-emission electron microscope equipped with an energy dispersive X-ray (EDX) spectrometer (Oxford Instruments X-Max Xtreme, 100 mm^2, 1–5 kV). Thermogravimetric analysis (TGA) was conducted by means of a NETZSCH TG 209 F1 libra under oxygen atmosphere and with a heating rate of 3 °C min^{-1} from room temperature to 600 °C. Powder X-ray diffraction (XRD) patterns were collected with an automated Philips Bragg-Brentano diffractometer equipped with a graphite monochromator. The long-fine focus Cu tube was operated at 40 kV and 25 mA. The diffractograms were recorded in a 2θ range from 20° to 140° with a 0.03° step size and 14 s acquisition time. The diffractograms were refined using the GSAS software.[29] The peak shape was modeled with a Pseudo-Voigt function and both Gaussian and Lorentzian broadening were taken into account for refining the FWHM (full width at half maximum) as a function of 2θ. The $P6_3mc$ space group and the starting atomic coordinates of the model by Xu and Ching[30] were chosen for the refinement, with the initial values for the isotropic temperature factors (U_{iso}) arbitrarily chosen as 0.025 Å^2. The oxygen sites were designated fully occupied, while constraints for fractional occupancies for Mn and Zn were used according to the stoichiometry of the synthesized samples. A 9-terms polynomial function was utilized to model the background. The cell parameters, scale factor, and the background polynomial function were free variables during the refinement. The parameters were added stepwise to the refinement in the following order: 2θ zero-shift, peak shape, peak asymmetry, atomic coordinates, and isotropic thermal factor. Final convergence was assumed to be reached when the parameter shifts were <1% of their estimated standard deviation.

X-ray absorption spectroscopy (XAS) was performed at the Mn and Zn K-edge at the BM25 SpLine Spanish CRG Beamline of the European Synchrotron Radiation Facility (ESRF, Grenoble, France). The storage ring was operated at 6 GeV in a uniform filling mode with a maximum electron current of 200 mA. The white beam, delivered by the bending magnet source, was monochromatized with a fixed-exit double-crystal Si(111) monochromator. A bender curved the second crystal sagittally in order to dynamically focus the beam. The first monochromator crystal was ethanol-cooled, while the second crystal was kept at room temperature. The second crystal was equipped with a long-travel piezoelectric actuator (Nexline-inchworm PI) that allowed changing the Bragg angle slightly (pitch adjustment) in order to reduce the harmonic content of the beam if necessary. The position and dimension of the focused beam are kept constant during a ~1 keV energy scan, which represents standard conditions for an extended X-ray absorption fine structure (EXAFS) measurement. In this configuration, the beam size at the sample was about 2 × 2 mm^2. XAS spectra were obtained in transmission mode using two ionization chambers (I_0 and I_1) filled with nitrogen and argon at different pressures to achieve the optimal efficiency in the targeted energy range (with 20% and 80% absorption, respectively). The XAS spectra were recorded at room temperature up to 1,000 eV above the given edge, with a constant energy step of 0.8 eV and 0.2 eV for Zn and Mn, respectively, in the X-ray absorption near edge structure (XANES) region and 0.05 Å^{-1} steps in the EXAFS

region, as well as an acquisition time of 2 s per point. The evaluated noise level was of the order of 2·10^{-4} for all the spectra. XAS spectra of Mn (6,539 eV) and Zn (9,659 eV) metal foils, serving as reference and being placed in a second experimental chamber after the sample, were acquired simultaneously with each scan for continuous monitoring of the energy scale against possible monochromator instabilities. No drifts of the energy scale were observed during the experiments. The edge energy was taken as the first maximum of the first derivative of the spectra. The XAS spectra were processed using the Demeter package.[31] Normalization, background subtraction, energy calibration, and spectra alignment were performed using the Athena software. The k^2-weighted EXAFS spectra $\chi(k)$ were further Fourier-transformed in a k-range of 2.0–12.0 Å^{-1} for the Zn spectra and 2.0–10.0 Å^{-1} for the Mn spectra with a Kaiser-Bessel window function. Shell fitting was performed using the Artemis software and the theoretical backscattering amplitudes and phase shifts were calculated using the FEFF6 code.[32] The spectra at the Zn K-edge were fit in the R-space in a range of 1.0–4.5 Å and all the single scattering contributions as well as the multiple scattering contributions of significance were included in the fit up to the cut-off distance, which included coordination shells up to the 3rd one. The spectra at the Mn K-edge were fit in an R range of 1.0–3.5 Å for the oxidic samples and in a range of 1.0–3.0 Å for the metallic samples. The fitting parameters were the scattering path length R and the Debye-Waller factor σ^2 for each path, the E_0 shift, and the amplitude reduction factor S_0^2. The latter was, in the case of the Mn spectra, determined to be 0.7 by fitting a $MnCO_3$ reference spectrum with the corresponding theoretical model and kept constant for the fitting of the Mn K-edge EXAFS spectra.

The ab initio simulation of the XANES spectra was performed by means of the FDMNES software.[33] The Mn K-edge spectra were calculated in the photoelectron energy range of $-1.0 < E < 120.0$ eV with respect to the Fermi energy level. The Hedin-Lundqvist complex potential[34] was used to calculate the excited states. Clusters of 5.0 Å around each non-equivalent absorbing atom, the space group symmetry, and the Muffin-Tin (MT) approximation were considered for the XANES simulation. MnO_2, Mn_2O_3, and MnO spectra were calculated by considering the $P4_2/mnm$ (a = 4.458 Å, c = 2.942 Å), Ia-3 (a = 9.617 Å), and the Fm-3m (a = 4.495 Å) space group, respectively. The Mn-doped ZnO structure was manually created by considering the ZnO lattice (space group $P6_3mc$, a = 3.289 Å, c = 5.307 Å), expanding the *ab* plane (2×), and replacing 1/8 of the Zn by Mn. The convolution parameters were kept constant. FDMNES is ab initio in the sense that it does not need any auxiliary parameters. Only the atomic positions are required and the code starts from the first-principles equations.

Electrochemical characterization.—Electrodes were prepared by mixing the active material (75 dry wt%), Super C65 (Imerys, 20 dry wt%), and sodium carboxymethyl cellulose (Na-CMC; Dow-Wolff Cellulosics, 5 dry wt%). The latter component was added as a 1.25 wt% aqueous solution. The resulting electrode slurries were homogenized using a planetary ball mill (Fritsch Vario-Planetary Mill Pulverisette 4) for 3 h at 400/−800 rpm employing 12 ml zirconia jars and zirconia balls. A laboratory-scale doctor blade (BYK Additive & Instruments) with a wet film thickness of 120 μm was used to cast the slurries onto dendritic copper foil (Schlenk). The electrode sheets were dried at room temperature overnight. Disk-shaped electrodes were cut using a 12 mm puncher (Hohsen). Subsequently, the electrodes were dried in a vacuum glass oven (Büchi B585) for 12 h at 120 °C. The electrode coating layer had a thickness of around 18 μm, corresponding to an active material mass loading of about 1.5–1.7 mg cm^{-2}. The test cells were assembled in an argon-filled glove box with water and oxygen levels kept below 0.1 ppm.

The electrochemical tests were performed in three-electrode Swagelok®-type cells with lithium metal (Honjo Metal Co.) serving as counter and reference electrodes. Glass fiber sheets (Whatman GF/D) with a diameter of 13 mm, dried at 160 °C for 48 h under

vacuum and used as separators, were drenched with the electrolyte solution, i.e., 1 M $LiPF_6$ in a mixture of ethylene carbonate and diethyl carbonate (EC/DEC, 3:7 wt%, UBE, battery grade). The cells were galvanostatically cycled by means of a battery cycler (Maccor). Cyclic voltammetry (CV) was conducted using a multi-channel potentiostat (Biologic VMP-3) with a sweep rate of 50 μV s^{-1} within a voltage range from 0.01 V to 3.0 V. The dis-/charge rate of 1 C is defined as 1,000 mA g^{-1}, considering the transformation of ZnO into the LiZn alloy and Li_2O and allowing for a direct comparison with previous studies on related materials. Unless specified otherwise, all specific capacity values reported in this study refer to the mass of the active material including the mass of the carbon coating in the case of $Zn_{0.9}Mn_{0.1}O$-C.

Operando electrochemical dilatometry.—For the *operando* electrochemical dilatometry measurements, the electrodes had a diameter of 10 mm. The tests were conducted in an ECD-3-nano setup from EL-CELL® with lithium as counter and reference electrode. The measurements were performed on a Biologic VMP-200 single-channel galvanostat/potentiostat at 20 °C.

Ex situ and operando XAS.—The electrodes for the ex situ XAS experiments were prepared with a dry mass ratio of 70 wt% of the active material, 20 wt% of Super C65, and 10 wt% of polyvinylidene fluoride (PVdF, Kynar 761, Arkema, dissolved in *N*-methyl pyrrolidone, Alfa Aesar). The resulting slurries were cast on carbon paper (QuinTech) with a wet film thickness of 300 μm. The electrodes had an active material mass loading of about 6.0 to 7.0 mg cm^{-2} in order to achieve sufficient absorption at both the Zn and Mn K-edge. The electrodes were cycled in three-electrode Swagelok®-type cells and stopped at the indicated potentials, disassembled in an argon-filled glove box, rinsed with dimethyl carbonate (DMC), and sealed in transparent poly(ethylene) (PE) foil to avoid ambient air contamination. The *operando* XAS experiments were conducted with the same electrodes, but assembled in pouch cells comprising lithium metal as counter electrode.

Operando XRD.—For the *operando* XRD measurements, slurries of 75 dry wt% of the active material, 20 dry wt% of Super C65, and 5 dry wt% of Na-CMC (1.25 wt.-% aqueous solution) were cast onto a beryllium window (Materion Brush) with a wet film thickness of 300 μm. The cell setup has been earlier reported by Bresser et al.[35] The beryllium disc serves simultaneously as the X-ray window and working electrode current collector. Lithium was used as counter electrode and the electrodes were separated by two sheets of Whatman GF/D drenched in 500 μl of 1 M $LiPF_6$ in EC:DEC (3:7). The measurements were performed on a Bruker D8 Advance diffractometer equipped with a copper tube (Cu Kα radiation, λ = 0.15406 nm) in Bragg-Brentano geometry, a 2θ range from 25° to 65°, a step size of 0.04°, and an overall time of 30 min for each scan. The cells were cycled with a dis-/charge rate of 0.05 C in a voltage range from 0.01 V to 3.0 V using a Biologic VMP-150 potentiostat at room temperature.

Results and Discussion

General physicochemical characterization.—$Zn_{0.9}Mn_{0.1}O$ was synthesized as reported earlier.[18,19] The synthesis is schematically illustrated in Fig. 1a. The solid mass obtained after evaporating the water was calcined at four different temperatures, i.e., at 360 °C, 400 °C, 450 °C, and 500 °C, in order to evaluate the influence of the calcination temperature. The XRD patterns of the resulting materials are presented in Fig. S1 (available online at stacks.iop.org/JES/168/030503/mmedia). The sample calcined at 500 °C shows apparent phase impurities of ilmenite $ZnMnO_3$. This is in good agreement with the literature, as it has been reported that elevated calcination temperatures for the synthesis of $Zn_{1-x}Mn_xO$ result in such a phase separation.[36] The sample calcined at 450 °C also shows such phase impurities—even though less pronounced. The samples calcined at

400 °C and 360 °C were both phase-pure and showed a rather similar crystallinity with respect to the intensity and width of the reflections. Nonetheless, the material calcined at 400 °C was selected for the following investigation, as well as the base for the carbon-coating step, since several of the performed experiments would benefit from a higher crystallinity. Figures 1b, 1c display SEM micrographs of $Zn_{0.9}Mn_{0.1}O$ and carbon-coated $Zn_{0.9}Mn_{0.1}O$ ($Zn_{0.9}Mn_{0.1}O$-C) at different magnifications as well as the corresponding EDX mapping for Mn and Zn. The average primary particle size of both materials is around 20 nm (compare also the insets), indicating that the carbon coating does not affect the particle size. The EDX mapping reveals that both Mn and Zn are homogeneously distributed over the secondary particles in both cases. The same is observed for carbon in the case of $Zn_{0.9}Mn_{0.1}O$-C (Fig. 1d). In fact, when comparing the SEM micrographs of $Zn_{0.9}Mn_{0.1}O$ (Fig. 1b) and $Zn_{0.9}Mn_{0.1}O$-C (Fig. 1c), it appears that the carbon is infiltrated into the space between the primary nanoparticles within the secondary particle agglomerates and, thus, not only covering the particles surface, but moreover linking the single particles and forming a percolating network within the secondary particles.[18] The overall carbon content was determined via TGA to be around 20 wt% (Fig. 1e). A detailed comparative XRD analysis and Rietveld refinement of $Zn_{0.9}Mn_{0.1}O$ and $Zn_{0.9}Mn_{0.1}O$-C is presented in Fig. 1f. The overall crystallinity increases slightly when the carbon coating is applied (see Table SI). This has been observed also for Fe-doped ZnO.[18] The unit cell parameters and disagreement indices for both materials, as well as for pure ZnO as Ref. 21, are summarized in Table SI. It has been shown previously that doping ZnO with an increasing amount of trivalent iron leads to an increase of the lattice parameter a_0 while c_0 decreases compared to pure ZnO.[21] In the case of $Zn_{0.9}Mn_{0.1}O$ and $Zn_{0.9}Mn_{0.1}O$-C, both a_0 and c_0 are increased in comparison to pure ZnO, resulting in an increased cell volume V_0. An explanation for this is the slightly larger ionic radius of Mn(II) in tetrahedral coordination (Zn(II): 0.6 Å, Mn(II): 0.66 Å).[37]

To investigate this in more detail, we performed XAS on the two samples. Figure 2a shows the normalized XANES spectra at the Zn K-edge for both $Zn_{0.9}Mn_{0.1}O$ and $Zn_{0.9}Mn_{0.1}O$-C. The spectra exhibit the typical spectral features (A, B, C) of tetrahedrally coordinated Zn^{2+} in wurtzite ZnO.[38,39] The oscillations in the case of $Zn_{0.9}Mn_{0.1}O$-C are slightly damped compared to $Zn_{0.9}Mn_{0.1}O$. However, both materials do not show any features of a different phase such as, for instance, ilmenite $ZnMnO_3$ or spinel-structure $ZnMn_2O_4$.[40] The Fourier-transformed EXAFS spectra (Fig. 2b) essentially represent the same shape. The Zn-O and Zn-Zn distances were determined by fitting the EXAFS spectra. The results are summarized in Table SII. Both compounds show comparable interatomic distances for the first and second coordination shells. The EXAFS Debye-Waller factor, σ^2, of $Zn_{0.9}Mn_{0.1}O$ is slightly lower than the one of $Zn_{0.9}Mn_{0.1}O$-C, indicating a slightly more distorted tetrahedron in the latter case.

Figure 3a displays the XANES spectra of $Zn_{0.9}Mn_{0.1}O$ and $Zn_{0.9}Mn_{0.1}O$-C at the Mn K-edge. In addition, reference spectra for Mn^{4+} (MnO_2), Mn^{3+} (Mn_2O_3), and Mn^{2+} ($MnCO_3$) are presented. Different from the spectra at the Zn K-edge, these spectra show clear differences for $Zn_{0.9}Mn_{0.1}O$ and $Zn_{0.9}Mn_{0.1}O$-C. A simple comparison of the XANES region with the given references reveals that $Zn_{0.9}Mn_{0.1}O$ has spectral similarities with MnO_2 and $Zn_{0.9}Mn_{0.1}O$-C has similarities with Mn_2O_3. Generally, Mn^{4+} and Mn^{3+} in MnO_2 and Mn_2O_3 prefer an octahedral coordination.[41] Therefore, it appears rather unlikely for both materials that manganese exclusively replaces tetrahedrally coordinated Zn^{2+} in the lattice. In fact, it has been shown that for $\times > 0.04$ in $Zn_{1-x}Mn_xO$, a phase separation towards the spinel-structured $ZnMn_2O_4$ containing Mn^{3+} in distorted octahedral coordination occurs.[40] However, the main absorption edge position of $Zn_{0.9}Mn_{0.1}O$ is below the one of MnO_2, and the main absorption edge position of $Zn_{0.9}Mn_{0.1}O$-C is below the one of Mn_2O_3 (Fig. S2). This indicates that the average oxidation states of Mn in $Zn_{0.9}Mn_{0.1}O$ and $Zn_{0.9}Mn_{0.1}O$-C are between 3+ and 4+ and between 2+ and 3+, respectively; in other words, manganese has
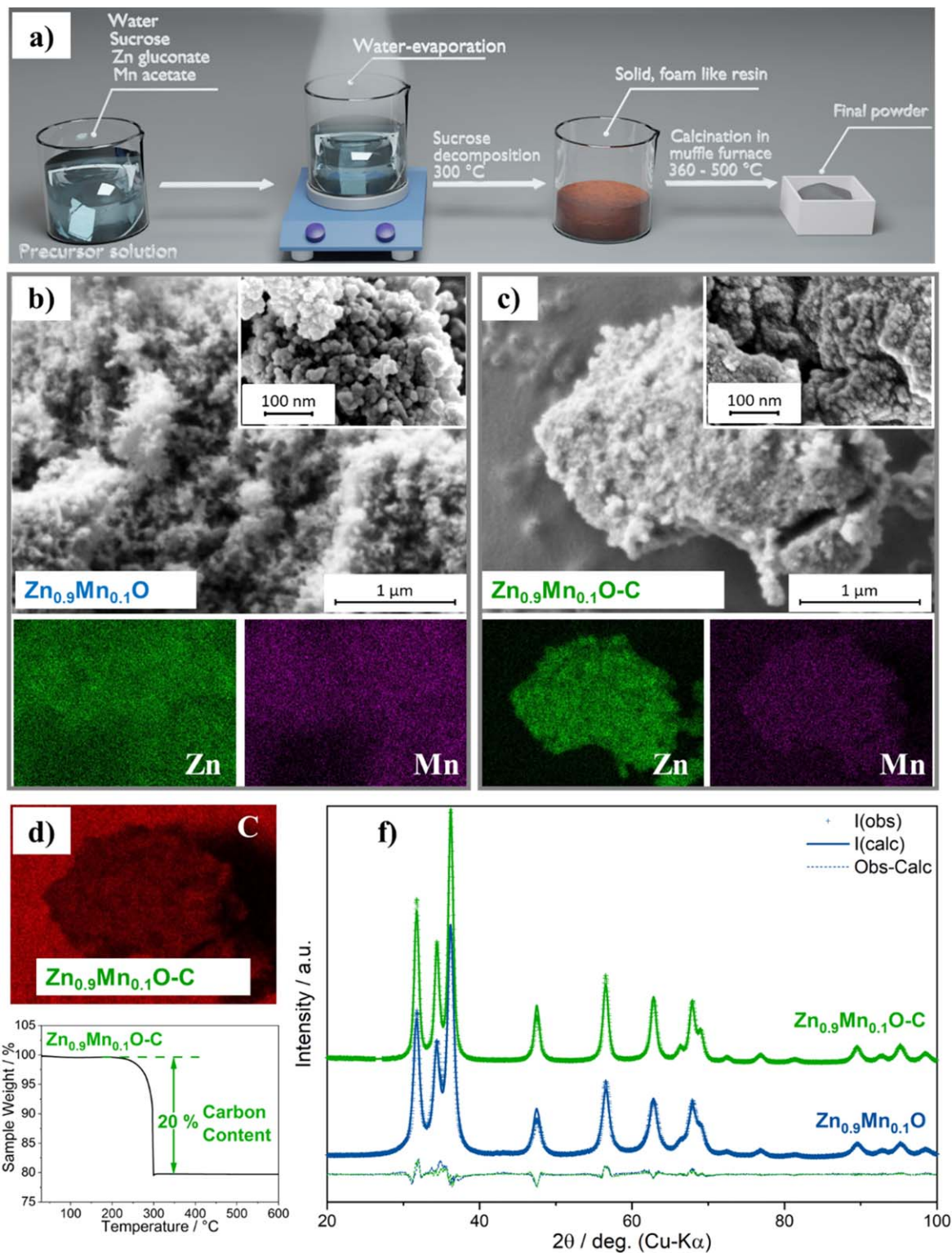
Figure 1. (a) Schematic illustration of the synthesis of $Zn_{0.9}Mn_{0.1}O$. (b,c) SEM micrographs and EDX mapping (Zn in green and Mn in purple) of (b) $Zn_{0.9}Mn_{0.1}O$ and (c) $Zn_{0.9}Mn_{0.1}O$-C with additional SEM micrographs at higher magnification as insets. (d) EDX mapping of carbon (in red) for $Zn_{0.9}Mn_{0.1}O$-C. (e) TGA for the determination of the mass of the carbon coating in $Zn_{0.9}Mn_{0.1}O$-C. (f) XRD patterns and Rietveld refinements of $Zn_{0.9}Mn_{0.1}O$ and $Zn_{0.9}Mn_{0.1}O$-C; the crosses represent the experimental data and the solid lines represent the calculated data.

been substantially reduced during the application of the carbon coating—and it has to be considered that XAS in this energy range is a bulk technique. A magnification of the pre-edge region is displayed in Fig. 3b and reveals substantial differences when comparing $Zn_{0.9}Mn_{0.1}O$ and $Zn_{0.9}Mn_{0.1}O$-C with the MnO_2 and Mn_2O_3

reference compounds. Especially the spectrum of $Zn_{0.9}Mn_{0.1}O$-C depicts a pronounced pre-edge feature, which is typical for Mn^{2+} in tetrahedral coordination due to the p-d hybridization and the increased probability of 1 s transitions to these hybridized orbitals.[42] This finding further supports the presence of different Mn species in
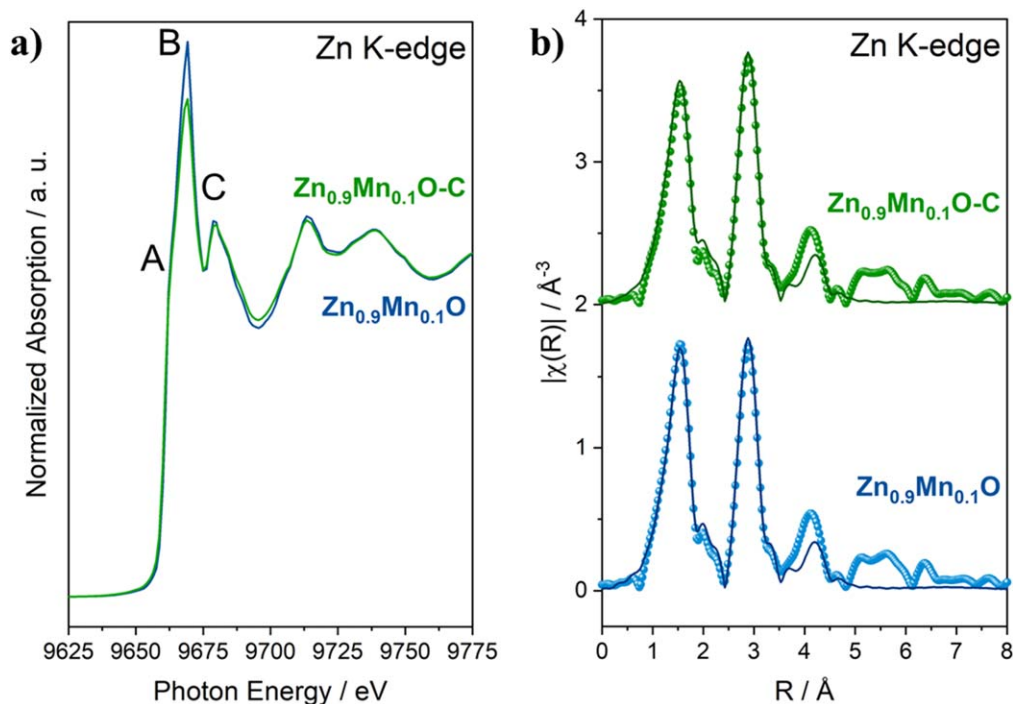
Figure 2. (a) XANES spectra of $Zn_{0.9}Mn_{0.1}O$ (blue) and $Zn_{0.9}Mn_{0.1}O$-C (green). (b) Fitted Fourier transform of the $k^2\chi(k)$ EXAFS spectra of the two samples (same color coding): the spheres represent the experimental data and the solid lines represent the best fit. The spectra were shifted vertically for the sake of clarity.
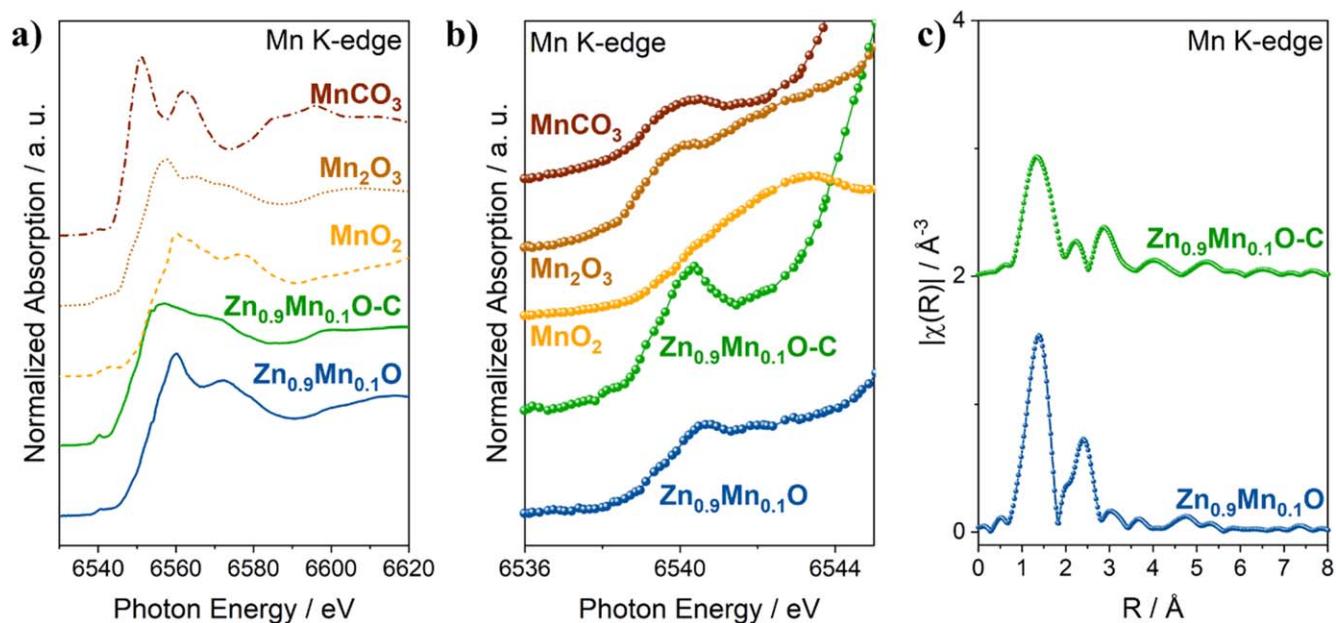
Figure 3. (a) Normalized XANES spectra at the Mn K-edge of $Zn_{0.9}Mn_{0.1}O$ (in blue), $Zn_{0.9}Mn_{0.1}O$-C (in green), MnO_2 (in yellow), Mn_2O_3 (in light brown), and $MnCO_3$ (in brown) and (b) a magnification of the pre-edge region. (c) The Fourier transform of the $k^2\chi(k)$ EXAFS spectra of $Zn_{0.9}Mn_{0.1}O$ and $Zn_{0.9}Mn_{0.1}O$-C. The spectra were shifted vertically for the sake of clarity.

$Zn_{0.9}Mn_{0.1}O$-C (and to a lesser extent also in $Zn_{0.9}Mn_{0.1}O$), which is in good agreement with mixed oxidation states of manganese in these samples. Moreover, the presence of Mn^{2+} in 4-fold coordination indicates that some of the manganese, indeed, replaces Zn^{2+} cations in the lattice—in particular in the case of $Zn_{0.9}Mn_{0.1}O$-C. In fact, as depicted in Fig. S3a, the spectrum of $Zn_{0.9}Mn_{0.1}O$-C can be fit by a linear combination of $Zn_{0.9}Mn_{0.1}O$ and the spectrum of an electrode based on $Zn_{0.9}Mn_{0.1}O$-C, which has been partially lithiated at 0.8 V (hereinafter

referred to as $Zn_{0.9}Mn_{0.1}O$-C-0.8 V—a more detailed discussion of the complete ex situ XAS analysis is provided later on). This partial lithiation results in the partial reduction of manganese to Mn^{2+}, as confirmed by the comparison with ab initio calculated XANES spectra for MnO_2, Mn_2O_3, MnO, and $Zn_{1-x}Mn_xO^{calc}$ (Figs. S3b, S3c). Accordingly, this sample is representative for the substitution of Zn^{2+} by Mn^{2+} in the crystal structure. The spectra of these two reference samples (i.e., $Zn_{0.9}Mn_{0.1}O$ and $Zn_{0.9}Mn_{0.1}O$-C-0.8 V) contribute with about 50%

each to the linear combination fit (LCF) of the spectrum of $Zn_{0.9}Mn_{0.1}O$-C, which corroborates the conclusion concerning the effect of the carbon coating. Further evidence for the extensive presence of tetrahedrally coordinated Mn^{2+} in $Zn_{0.9}Mn_{0.1}O$-C was obtained by comparing the Mn K-edge XANES of $Zn_{0.9}Mn_{0.1}O$ and $Zn_{0.9}Mn_{0.1}O$-C with the Fe K-edge spectrum of $Zn_{0.9}Fe_{0.1}O$-C and the Co K-edge spectrum of $Zn_{0.9}Co_{0.1}O$ (Fig. S4). In the latter two samples, zinc is replaced by iron or cobalt in the crystal structure[39] and the two samples show very similar spectral features as $Zn_{0.9}Mn_{0.1}O$-C, while the spectrum of $Zn_{0.9}Mn_{0.1}O$ shows significant differences concerning the position of the white line and the modulations after the white line. The Fourier-transformed EXAFS spectra at the Mn K-edge of $Zn_{0.9}Mn_{0.1}O$-C and $Zn_{0.9}Mn_{0.1}O$-C are depicted in Fig. 3c. The two spectra show significant differences, which is generally in line with the XANES spectra. We have performed a fitting with different reference structures, i.e., MnO_2, Mn_2O_3, Mn_3O_4, MnO, and $Zn_{1-x}Mn_xO^{calc}$ in order to determine the interatomic distances and the geometrical structure of Mn. Nevertheless, the results were rather poor with regard to the quality of the fit, revealing that no single reference compound satisfactorily represents the local surrounding of Mn in $Zn_{0.9}Mn_{0.1}O$ and $Zn_{0.9}Mn_{0.1}O$-C. In the case of $Zn_{0.9}Mn_{0.1}O$, though, the best fit was obtained with the model of MnO_2, with a large Debye-Waller factor for the second shell, indicating extensive structural distortion. In fact, when the coordination number is left variable, it shows rather low values of around 4 for the first coordination shell, i.e., values much lower than expected for MnO_2, as well as interatomic Mn-O distances of around 1.91 Å. This contradiction indicates that several different manganese species are present in the material. Considering also the absence of any MnO_2-related reflections in the XRD pattern (Fig. 1f), this suggests that Mn has mixed oxidation states, but a general preference to occupy octahedral sites in a distorted ZnO crystal. In the case of $Zn_{0.9}Mn_{0.1}O$-C, the fitting with Mn_3O_4 and $Zn_{1-x}Mn_xO^{calc}$ structural models shows equally good results, although both fits have rather high R factors of around 0.05. Nonetheless, this further supports the presence of both octahedrally and tetrahedrally coordinated Mn with an average oxidation state between 3+ and 2+.

To briefly summarize the structural characterization, the carbon coating leads to a reduced oxidation state of manganese and a modified coordination, i.e., a different position in the crystal structure. A precise determination of these characteristics, however, is at least very difficult. In fact, such difficulties have been reported also for a manganese-based cathode in a previous study.[43] Nonetheless, the most conceivable explanation of our findings is that manganese occupies both tetrahedral and octahedral sites in $Zn_{0.9}Mn_{0.1}O$-C and that the relative amount of tetrahedrally coordinated manganese is significantly higher compared to $Zn_{0.9}Mn_{0.1}O$.

Electrochemical characterization.—Figures 4a, 4b display the cyclic voltammetry (CV) data of electrodes based on $Zn_{0.9}Mn_{0.1}O$ (Fig. 4a) and $Zn_{0.9}Mn_{0.1}O$-C (Fig. 4b), investigated in a range from 0.01 V to 3.0 V in order to cover the whole electrochemically relevant voltage range. Both kinds of electrodes display four distinct regions after the initial electrolyte decomposition, labeled A (and A* after the first cyclic sweep), B, C, and D and representing the conversion, the alloying, the de-alloying, as well as the re-conversion reaction, respectively.[19] Generally, the CV data show essentially the same features as those reported earlier for pure ZnO,[19] indicating that the overall reaction mechanism is the same also when introducing manganese into the crystal structure. Major differences between the CV profiles of $Zn_{0.9}Mn_{0.1}O$ and $Zn_{0.9}Mn_{0.1}O$-C, especially after the first cyclic sweep, are: (i) a much broader current peak A/A*, which moreover has its maximum at lower potentials (especially after the first cyclic sweep), in the case of $Zn_{0.9}Mn_{0.1}O$-C; (ii) a more reversible de-/alloying reaction thanks to the carbon coating, as revealed by the greater reversibility of the

current response for the features B and C; and (iii) a much more reversible re-conversion reaction in the case of $Zn_{0.9}Mn_{0.1}O$-C, as indicated by the substantially enhanced reversibility of the current response for feature D. These differences are in line with the results reported earlier for Co-doped ZnO,[19] where cobalt occupies the same position as zinc in the crystal structure.[39] It appears that, in addition to the general benefits of the carbon coating (i.e., the enhanced electronic wiring within primary particle agglomerates and buffering effect), the position of the transition metal (TM) dopant in the crystal structure and/or its oxidation state play/s a decisive role. It appears also noteworthy that the cathodic peak A* appears at lower potentials compared to Co-doped ZnO, which is assigned to the lower redox potential of such manganese species compared to cobalt.[44]

The comparison of the dis-/charge profiles of electrodes based on $Zn_{0.9}Mn_{0.1}O$ (Fig. 4c) and $Zn_{0.9}Mn_{0.1}O$-C (Fig. 4d) confirms that de-/lithiation is much more reversible for the latter active material. This is particularly evident regarding the delithiation at elevated potentials, i.e., the reconversion reaction, but also at lower potentials, i.e., the dealloying reaction. This is in line with the previous statement concerning the lowered redox potential for the conversion-related cathodic peak of Mn-doped ZnO compared to Co-doped ZnO. Also interesting to note is that the comparison of the dis-/charge profile of Mn-doped ZnO with Fe-doped ZnO reveals essentially the same finding (Fig. S5). In fact, the average lithiation potential is slightly lower, especially in the elevated voltage region where the reduction of the transition metal occurs,[21] while the two profiles essentially overlap afterwards. On the other hand, the delithiation voltage of Mn-doped ZnO is lower than the delithiation voltage of Fe-doped ZnO across the whole delithiation process under the given experimental conditions. This finding further supports the important impact of the choice of the TM dopant on the average de-/lithiation potential—as observed earlier for TM-doped SnO_2.[23,24] The continuous galvanostatic cycling at 0.1 C (1 C = 1,000 mA g^{-1}), depicted in Fig. 4e, shows that electrodes based on both active materials $Zn_{0.9}Mn_{0.1}O$ and $Zn_{0.9}Mn_{0.1}O$-C provide superior specific capacities and cycling stability compared to pure ZnO. However, the carbon coating results in substantially higher specific capacities (about 200 mAh g^{-1}). Additionally, a substantial improvement in Coulombic efficiency is observed, especially during the initial cycles, but also after 80 cycles (i.e., 99.3% vs 98.9%), which is assigned to the interface-stabilizing effect of the carbon coating.[45] When subtracting the mass of the carbon coating, the specific capacity reaches values close to the theoretical maximum of 967 mAh g^{-1} in the initial cycles. Such substantial improvement compared to uncoated $Zn_{0.9}Mn_{0.1}O$, i.e., an increase in capacity by about 400 mAh g^{-1}, appears unlikely to originate from the beneficial effects of the carbon coating only. In fact, a previous study on Fe-doped ZnO did not show such a great improvement in capacity after applying a carbon coating, but rather an enhancement in capacity retention and rate capability.[18] The large capacity enhancement further indicates the beneficial impact of tetrahedrally coordinated manganese replacing zinc in the crystal structure occurring upon carbon-coating. Besides, electrodes based on $Zn_{0.9}Mn_{0.1}O$-C also show good rate capability (Fig. 4f). When increasing the dis-/charge rate from 0.1 C to 1 C, the specific capacity decreases by only 138 mAh g^{-1} from 740 mAh g^{-1} to 602 mAh g^{-1}. After the rate test, the electrodes recover essentially the same capacity as prior to the rate test—even slightly higher values, which is attributed to the quasi-reversible formation of the solid electrolyte interphase.[45]

Investigation of the Li^+ storage mechanism—operando experiments.—To investigate the origin of the superior reversibility of the de-/lithiation reaction of $Zn_{0.9}Mn_{0.1}O$-C in more detail, several *operando* experiments were conducted. The results are summarized in Fig. 5. In Figs. 5a, 5b, the *operando* dilatometry data are presented for $Zn_{0.9}Mn_{0.1}O$ and $Zn_{0.9}Mn_{0.1}O$-C, respectively. The dilatation upon the initial lithiation is 20.1% for $Zn_{0.9}Mn_{0.1}O$ and 17.4% for $Zn_{0.9}Mn_{0.1}O$-C. While this finding already reveals the beneficial impact of the carbon coating, one has to consider that the content of
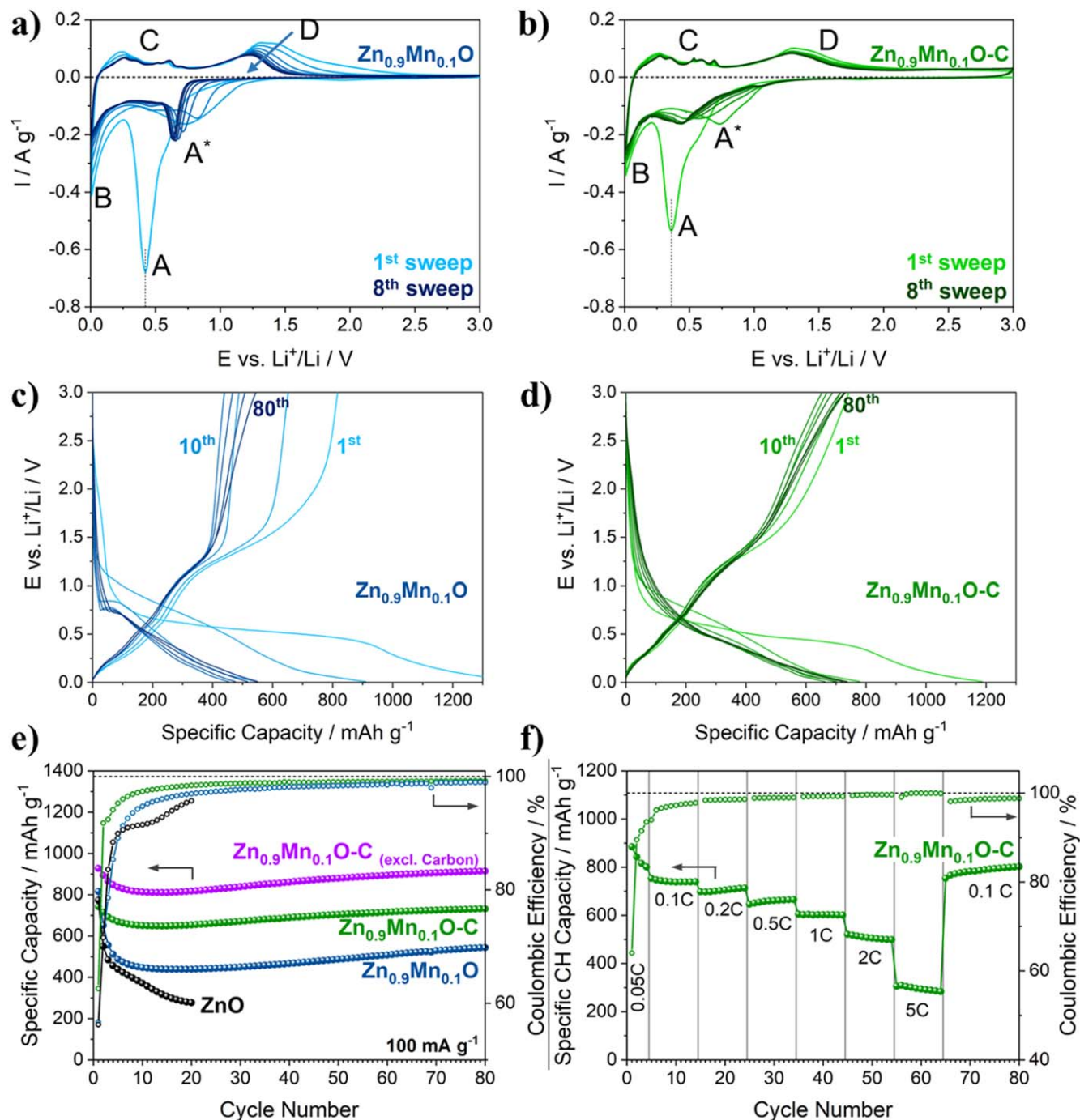
**Figure 4.** (a), (b) Cyclic voltammograms of electrodes based on (a) $Zn_{0.9}Mn_{0.1}O$ and (b) $Zn_{0.9}Mn_{0.1}O$-C. (c) (d) Galvanostatic dis-/charge profiles for each tenth cycle for electrodes based on (c) $Zn_{0.9}Mn_{0.1}O$ and (d) $Zn_{0.9}Mn_{0.1}O$-C (dis-/charge rate: 1st cycle at 0.05 C, subsequent cycles at 0.1 C (1 C = 1,000 mA g^{-1}). (e) Comparative plot of the specific capacity vs the cycle number for electrodes based on ZnO (in black), $Zn_{0.9}Mn_{0.1}O$ (in blue), and $Zn_{0.9}Mn_{0.1}O$-C (in green; dis-/charge rate: 1st cycle at 0.05 C, subsequent cycles at 0.1 C); in addition, the specific capacity for the electrodes based on $Zn_{0.9}Mn_{0.1}O$-C when subtracting the mass of the carbon coating is shown (in purple). (f) Rate performance of electrodes based on $Zn_{0.9}Mn_{0.1}O$-C at varying dis-/charge rates from 0.1 C to 5 C.

$Zn_{0.9}Mn_{0.1}O$ is relatively smaller in the carbon-coated material, since the mass ratio for the electrode preparation includes also the carbon coating. More important for the cycling stability, in fact, is the subsequent electrode thickness variation. For both kinds of electrodes, it is generally decreasing upon cycling. The reversible dilatation averages to about 4% for both $Zn_{0.9}Mn_{0.1}O$ and $Zn_{0.9}Mn_{0.1}O$-C. However, the irreversible fraction, assigned to ongoing electrolyte decomposition and structural changes,[45,46] is larger for $Zn_{0.9}Mn_{0.1}O$, resulting in a continuous increase in electrode thickness. Accordingly, it is concluded that the carbon coating helps to maintain the integrity of the electrode during cycling

by buffering the occurring volume changes and in turn stabilizing the long-term cycling.

In a next step, we performed *operando* XRD for the two samples (Figs. 5c, 5d). The data obtained for electrodes based on $Zn_{0.9}Mn_{0.1}O$ (Fig. 5c) show the typical lithiation and delithiation process of ZnO: An initial conversion to Zn^0 and Mn^0, indicated by the gradual decrease in intensity of the ZnO-related reflections and the appearance of reflections related to the formation of metallic species. Subsequently, the metallic zinc alloys with lithium, forming Li$_x$Zn with $\times \leqslant 1$. The corresponding reflections, however, are very broad, suggesting very small nanograins and/or a low crystallinity. These observations are in line with previous
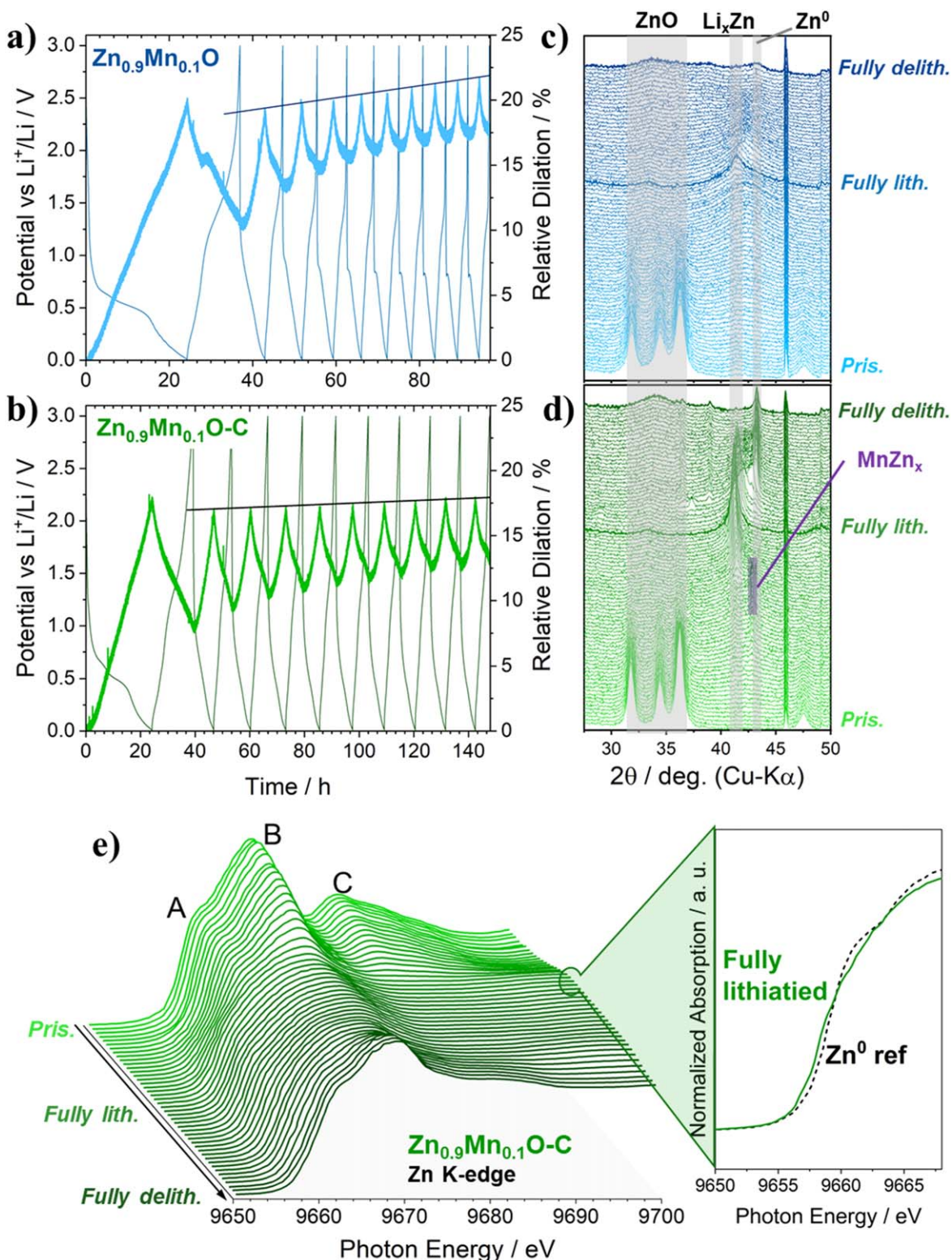
Figure 5. Operando dilatometry of (a) $Zn_{0.9}Mn_{0.1}O$ and (b) $Zn_{0.9}Mn_{0.1}O$-C. Dis-/charge rate: first cycle at 0.05 C and subsequent cycles at 0.1 C (1 C = 1000 mA g^{-1}). Operando XRD of (c) $Zn_{0.9}Mn_{0.1}O$ and (d) $Zn_{0.9}Mn_{0.1}O$-C, where the main reflections for the analysis are marked with gray and orange bars. (e) Operando XANES at the Zn K-edge of $Zn_{0.9}Mn_{0.1}O$-C. Dis-/charge rate: 0.1 C. (f) Comparison of the spectrum recorded for the fully lithiated state and a Zn^{0} reference.

studies on Fe-doped ZnO[18] and Co-doped ZnO,[19] where they were attributed to the enhanced electronic conductivity due to the presence of metallic Fe or Co and a confinement effect. Accordingly, the introduction of manganese appears to have a similarly beneficial effect in comparison to pure ZnO.[19] At the end of the subsequent delithiation, i.e., in the fully delithiated state, only a very broad reflection is observed in the region of the three major ZnO-related reflections, showing that the material remains essentially (quasi-)amorphous.
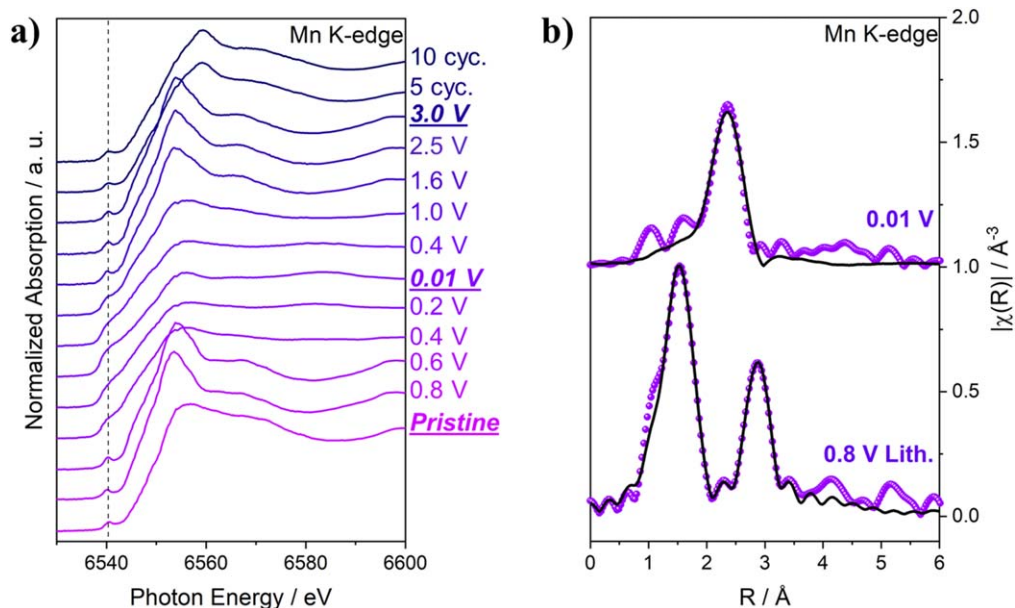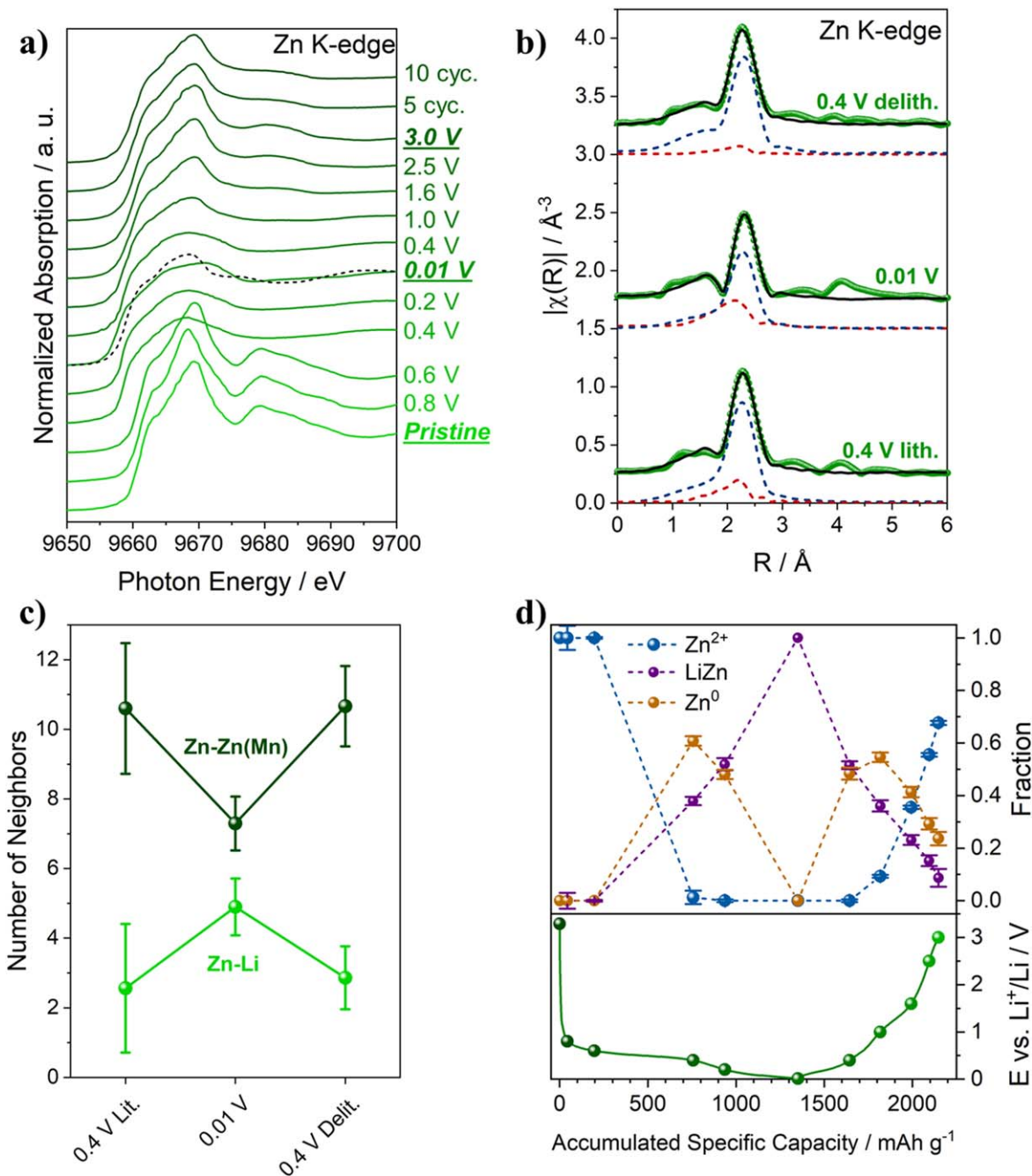
Figure 6. (a) Normalized ex situ XANES spectra at the Mn K-edge of electrodes based on $Zn_{0.9}Mn_{0.1}O$-C, stopped at different potentials during the first cycle and after 5 and 10 complete dis-/charge cycles. The spectra were shifted vertically for the sake of clarity. (b) Fourier transform of the $k^2\chi(k)$ EXAFS spectra of the electrodes stopped at 0.8 V upon lithiation and in the fully lithiated state, i.e., at 0.01 V. The purple spheres represent the experimental data and the solid black lines represent the best fit. The fit for the spectrum at 0.8 V was performed in the range of R = 1.0–3.5 Å, and the fit for the spectrum at 0.01 V was performed in the range of R = 1.0–3.0 Å.

In the case of $Zn_{0.9}Mn_{0.1}O$-C (Fig. 5d), the general evolution of the structure is similar, but the reflections are much more defined. Initially, the reflections of the ZnO phase gradually decrease in intensity, and a broad reflection emerges in the 2θ range of around 42.5°, originating from the initial reduction to Zn^0 and Mn^0. The first rather pronounced reflection at 42.8° matches with a $MnZn_x$ alloy— similarly to the $FeZn_x$ alloy formation occurring in carbon-coated $Zn_{0.9}Fe_{0.1}O$.[22] This is remarkable, as there has been no indication for the formation of such alloy for $Zn_{0.9}Mn_{0.1}O$, suggesting that the initial crystal lattice site of manganese makes the difference here. Upon further lithiation, the Li_xZn alloy (with x < 1, potentially comprising also some manganese) forms, matching the PDF reference 03–065 for the LiZn alloy in the fully lithiated electrode. During the subsequent delithiation, this reflection is shifting towards higher angles, indicating a gradual de-alloying with $0 \leqslant x \leqslant 1$ in Li_xZn. Interestingly, the $MnZn_x$ alloy is not observed upon further delithiation, while clear reflections related to the formation of hexagonal Zn^0 appear at 43.2°. Eventually, only a very broad reflection is observed in the region of the major ZnO reflections, revealing that also for the carbon-coated sample the material remains (quasi-)amorphous, just like for $Zn_{0.9}Mn_{0.1}O$.

As such (quasi-)amorphous materials are not accessible anymore by means of XRD, we complemented our investigation by *operando* XANES spectroscopy to follow the electronic and local structural changes. The results obtained for $Zn_{0.9}Mn_{0.1}O$-C at the Zn K-edge are depicted in Fig. 5e. Generally, the spectral features A, B, and C vanish upon lithiation and the eventually recorded spectrum in the fully lithiated state reveals a main absorption edge that is shifted below the one of metallic zinc (see also the inset in Fig. 5e). This is ascribed to the formation of the LiZn alloy.[47] Upon delithiation, the spectral features A, B, and C of the oxide phase are partially recovered, indicating that there is a substantial fraction of zinc that is reoxidized to ZnO, despite the very poor long-range ordering as found by means of *operando* XRD. This finding is analyzed in more detail in the following section, presenting the ex situ XANES and EXAFS results.

Investigation of the Li^+ storage mechanism—Ex situ XANES and EXAFS.—An ex situ XANES and EXAFS analysis of

$Zn_{0.9}Mn_{0.1}O$-C was performed to investigate the electronic and local-scale structural changes upon de-/lithiation. Figure S6 shows an exemplary dis-/charge profile with an indication of the potentials at which the cells had been stopped and disassembled in order to recover the electrodes. The corresponding XANES spectra at the Mn K-edge are presented in Fig. 6a. As discussed earlier, though still being quite remarkable, manganese is significantly reduced already at 0.8 V upon the initial lithiation and the spectrum qualitatively matches very well the calculated spectrum $Zn_{1-x}Mn_xO^{calc}$, for which we assumed that all manganese is divalent and replacing the divalent zinc cations in the crystal structure (see Figs. S3b, S3c).[38] The spectrum remains essentially unchanged at 0.6 V. Starting from 0.4 V, manganese appears to be fully metallic (either in the form of Mn^0 and/or as $MnZn_x$) and remains metallic until the fully lithiated state at 0.01 V. Figure 6b provides a comparison of the EXAFS spectra at the Mn K-edge of the $Zn_{0.9}Mn_{0.1}O$-C-based electrodes stopped at 0.8 V and at 0.01 V. The spectrum of the electrodes discharged to 0.8 V, i.e., a very early lithiation stage, is fit best with the structural model of $Zn_{1-x}Mn_xO^{calc}$, further corroborating the presence of divalent manganese substituting tetrahedrally coordinated divalent zinc cations in the lattice (see Table SIII for the results of the fitting). Nonetheless, the Debye-Waller factor, σ^2, and the corresponding range of error for the Mn-Zn(Mn) coordination is rather high with 0.015(13), suggesting structural disorder in the second coordination shell.[39] The EXAFS spectrum of the fully lithiated electrode shows only one peak, corresponding to metallic manganese. The results of the fit (Table SIII) reveal that the coordination number of Mn-Mn neighbors is drastically reduced from 12 in α-Mn[48] to around 6. Such a substantial decrease has been assigned to the presence of very small and defective metallic clusters,[49] which is in agreement with the anticipated formation of very fine transition metal nanograins in such materials, favoring the electron transport within the nanoparticles.[18,19] Upon delithiation, Mn stays metallic essentially up to 1.0 V (Fig. 6a). Nevertheless, when further delithiating the electrode, manganese is oxidized again and eventually appears to be reoxidized up to Mn^{2+} in the completely delithiated state at 3.0 V. The good match with the spectrum recorded for the electrode which has been discharged to 0.8 V indicates that manganese prefers to remain tetrahedrally

Figure 7. (a) Normalized ex situ XANES spectra at the Zn K-edge of electrodes based on $Zn_{0.9}Mn_{0.1}O$-C stopped at different potentials during the first cycle and after 5 and 10 complete dis-/charge cycles. The spectra were shifted vertically for the sake of clarity. (b) Fourier transform of the $k^2\chi(k)$ EXAFS spectra collected at the Zn K-edge of electrodes stopped at 0.4 V upon lithiation, at 0.01 V (fully lithiated), and at 0.4 V upon delithiation. The spectra were shifted vertically for the sake of clarity. The green spheres represent the experimental data and the solid black lines represent the best fit. Contributions of Li-Zn (in red) and Zn-Zn (in blue) are shown as dashed lines. The spectra have not been phase corrected and the peak positions, therefore, do not represent the actual interatomic distances. (c) Results of the EXAFS fits for the nearest neighbors of Zn with different contributions of the Zn-Zn(Mn) coordination (dark green) and the Zn-Li coordination (bright green). The fits were performed in the range of R = 1.0–3.0 Å. (d) LCF results for the spectra shown in (a) using the spectra of the pristine electrode, the electrode discharged to 0.01 V, and the metallic zinc reference as standards for Zn^{2+} (in blue), the LiZn alloy (in purple), and metallic zinc (in orange), respectively.

coordinated within the zinc oxide lattice. Similarly, the pre-edge peak recovers the initial intensity as well, supporting the previous statement. After 5 and 10 cycles, however, manganese is further oxidized to oxidation states higher than 2+. This increase in oxidation state, which has been reported also for other manganese-containing compounds such as $ZnMn_2O_4$[50] and manganese silicate,[51] is presumably accompanied by the transition to an octahedral coordination with regard to the earlier discussed findings

and, thus, might explain the initial decrease in capacity (compare Figs. 4e, 4f).

To further elucidate the reversibility of the de-/lithiation reaction, we conducted an ex situ XANES study also at the Zn K-edge (Fig. 7). Following a rather qualitative analysis, it appears that ZnO is the main zinc species until 0.6 V (Fig. 7a). Upon further lithiation at lower potentials and along the slightly sloping voltage plateau (Fig. S6), zinc is reduced to the metallic state, as revealed by the

comparison of the XANES spectrum recorded at 0.4 V with the reference spectrum for metallic zinc—both showing the same energy at the edge (Fig. S7). The oscillations after the edge, however, are substantially damped for the ex situ spectrum compared to the reference spectrum. This might be related to the rather small grains formed, the formation of the MnZn$_x$ alloy, as found by *operando* XRD (Fig. 5d), and/or an initial alloying with lithium. At 0.01 V, i.e., in the fully lithiated state, the edge position shifts to lower energies than that of metallic zinc, which is assigned to the formation of LiZn, i.e., an alloy phase with a relatively high lithium content.[47] Upon delithiation, the spectrum of the electrode charged to 0.4 V is very similar to that obtained for the electrode discharged (lithiated) to 0.4 V, especially with regard to the edge position (see also Fig. S7), indicating that the oxidation state is essentially the same.

The Fourier-transformed EXAFS spectra of electrodes, which were stopped at 0.4 V upon lithiation, 0.01 V, and 0.4 V upon delithiation, are presented in Fig. 7b. All three spectra show one main peak, corresponding to Zn^0 and/or a Li$_x$Zn alloy. The spectrum of the electrode discharged to 0.01 V, however, shows a slightly more damped amplitude compared to the other two electrodes. This indicates a higher amount of weakly scattering lithium in the alloy. In fact, the results of the fit of the coordination number, presented in Fig. 7c, confirm that the Li$_x$Zn alloy is present already at 0.4 V upon lithiation and still present at 0.4 V upon delithiation. The final alloy phase shows a Li:Zn ratio of around 0.83:1, which is close to the theoretical maximum ratio of 1:1.

During the delithiation above 0.4 V, i.e., at 1.0 V and beyond (Fig. 7a), the oxide phase starts to reform and when the electrode is fully delithiated at 3.0 V, the spectral features of the ZnO phase are recovered—although with increasingly damped oscillations upon cycling as observed for the spectra recorded for electrodes after 5 and 10 cycles. Generally, this finding is in agreement with the *operando* XANES data and indicates that the fraction of reoxidized zinc is rather high. For a quantification of the amount of reoxidized zinc, we performed LCF of the XANES spectra. The spectra of the pristine electrode, the electrode discharged to 0.01 V, and the metallic zinc reference were used as standards, being representative for divalent zinc, the LiZn alloy, and metallic zinc, respectively. Given these standards, we will refer to both metallic zinc and the MnZn$_x$ alloy simply as Zn^0 in the following, since we cannot differentiate between the two. The best results of the LCF are presented in Fig. 7d. At 0.4 V, both Zn^0 and a LiZn alloy are present. This corroborates the abovementioned XANES and EXAFS data, which indicate that some alloying occurs already along the voltage plateau. At 0.2 V upon lithiation and at 0.4 V upon delithiation, the ratio between LiZn and Zn^0 is 1:1. Around 70% of the comprised zinc is reoxidized to zinc oxide at 3.0 V, which is a substantially greater percentage than what has been reported earlier for pure ZnO[47] and, thus, underlining the beneficial impact of the manganese doping and carbon coating.

Conclusions

Based on a comprehensive physicochemical and electrochemical characterization it has been shown that the manganese-doping of zinc oxide generally enables an improved cycling stability and higher specific capacities compared to pure zinc oxide. The additional application of a carbon coating leads to a decreased oxidation state of manganese, resulting in an increased preference for a tetrahedral coordination and replacement of the zinc cation in the crystal structure. These changes, in combination with the general benefits of the carbon coating, enable further enhanced specific capacities, approaching the theoretical maximum (when excluding the mass of the carbon coating). Following an extensive combination of complementary ex situ and *operando* techniques, this improvement originates from a decreased volume variation upon cycling and an enhanced reversibility of the conversion reaction, i.e., an increased reoxidation of manganese and zinc—presumably triggered

by the intermediate formation of an MnZn$_x$ alloy during lithiation. We may anticipate that these findings will contribute to the further improved understanding of the de-/lithiation mechanism in conversion/alloying materials.

ORCID

Tobias Eisenmann https://orcid.org/0000-0002-0543-2465
Adele Birrozzi https://orcid.org/0000-0002-5777-2277
Angelo Mullaliu https://orcid.org/0000-0003-2800-2836
Gabriele Giuli https://orcid.org/0000-0002-2984-5045
Angela Trapananti https://orcid.org/0000-0001-7763-5758
Stefano Passerini https://orcid.org/0000-0002-6606-5304
Dominic Bresser https://orcid.org/0000-0001-6429-6048

References

1. R. Wagner, N. Preschitschek, S. Passerini, J. Leker, and M. Winter, *J. Appl. Electrochem.*, **43**, 481 (2013).
2. M. Armand et al., *J. Power Sources*, **479**, 228708 (2020).
3. J. Asenbauer, T. Eisenmann, M. Kuenzel, A. Kazzazi, Z. Chen, and D. Bresser, *Sustain. Energy Fuels*, **4**, 5387 (2020).
4. W. J. Zhang, *J. Power Sources,*, **196**, 13 (2011).
5. M. N. Obrovac and V. L. Chevrier, *Chem. Rev.*, **114**, 11444 (2014).
6. N. Nitta and G. Yushin, *Part. Part. Syst. Charact.*, **31**, 317 (2014).
7. D. Liu, Z. J. Liu, X. Li, W. Xie, Q. Wang, Q. Liu, Y. Fu, and D. He, *Small*, **13**, 1702000 (2017) .
8. C. Liang, M. Gao, H. Pan, Y. Liu, and M. Yan, *J. Alloys Compd.*, **575**, 246 (2013).
9. R. A. Huggins, *J. Power Sources,*, **81–82**, 13 (1999).
10. J. Cabana, L. Monconduit, D. Larcher, and M. R. Palacín, *Adv. Mater.*, **22**, 170 (2010).
11. M. D. Bhatt and J. Y. Lee, *Int. J. Hydrogen Energy*, **44**, 10852 (2019).
12. N. Loeffler, D. Bresser, S. Passerini, and M. Copley, *Johnson Matthey Technol. Rev.*, **59**, 34 (2015).
13. V. Aravindan, Y. S. Lee, and S. Madhavi, *Adv. Energy Mater.*, **5**, 1402225 (2015).
14. I. A. Courtney and J. R. Dahn, *J. Electrochem. Soc.*, **144**, 2045 (1997).
15. Y. Idota, T. Kubota, A. Matsufuji, Y. Maekawa, and T. Miyasaka, *Science*, **276**, 1395 (1997).
16. Z.-W. Fu, F. Huang, Y. Zhang, Y. Chu, and Q.-Z. Qin, *J. Electrochem. Soc.*, **150**, A714 (2003).
17. D. Bresser, S. Passerini, and B. Scrosati, *Energy Environ. Sci.*, **9**, 3348 (2016).
18. D. Bresser, F. Mueller, M. Fiedler, S. Krueger, R. Kloepsch, D. Baither, M. Winter, E. Paillard, and S. Passerini, *Chem. Mater.*, **25**, 4977 (2013).
19. F. Mueller, D. Geiger, U. Kaiser, S. Passerini, and D. Bresser, *Chem. Electro. Chem*, **3**, 1311 (2016).
20. F. Mueller, A. Gutsche, H. Nirschl, D. Geiger, U. Kaiser, D. Bresser, and S. Passerini, *J. Electrochem. Soc.*, **164**, A6123 (2017).
21. G. Giuli, T. Eisenmann, D. Bresser, A. Trapananti, J. Asenbauer, F. Mueller, and S. Passerini, *Materials*, **11**, 49 (2017).
22. J. Asenbauer, A. Hoefling, S. Indris, J. Tübke, S. Passerini, and D. Bresser, *ACS Appl. Mater. Interfaces*, **12**, 8206 (2020).
23. Y. Ma, Y. Ma, G. Giuli, T. Diemant, R.-J. Behm, D. Geiger, U. Kaiser, U. Ulissi, S. Passerini, and D. Bresser, *Sustain. Energy Fuels*, **2**, 2601 (2018).
24. A. Birrozzi, J. Asenbauer, T. E. Ashton, A. R. Groves, D. Geiger, U. Kaiser, J. A. Darr, and D. Bresser, *Batter. Supercaps*, **3**, 284 (2020).
25. M. Kuenzel, H. Choi, F. Wu, A. Kazzazi, P. Axmann, M. Wohlfahrt-Mehrens, D. Bresser, and S. Passerini, *Chem. Sus. Chem*, **13**, 2650 (2020).
26. J. Asenbauer, J. R. Binder, F. Mueller, M. Kuenzel, D. Geiger, U. Kaiser, S. Passerini, and D. Bresser, *Chem. Sus. Chem*, **13**, 3504 (2020).
27. J. Asenbauer, A. Varzi, S. Passerini, and D. Bresser, *J. Power Sources*, **473**, 228583 (2020).
28. L. Wang, K. Tang, M. Zhang, and J. Xu, *Nanoscale Res. Lett.*, **10**, 1 (2015).
29. A. C. Larson and R. B. Von Dreele, *Los Alamos Natl. Lab. Rep. LAUR* (2004)86.
30. Y.-N. Xu and W. Y. Ching, *Phys. Rev. B*, **48**, 4335 (1993).
31. B. Ravel and M. Newville, *J. Synchrotron Radiat.*, **12**, 537 (2005).
32. S. I. Zabinsky, J. J. Rehr, A. Ankudinov, R. C. Albers, and M. J. Eller, *Phys. Rev. B*, **52**, 2995 (1995).
33. Y. Joly, *Phys. Rev. B - Condens. Matter Mater. Phys.*, **63**, 125120 (2001).
34. L. Hedin, B. I. Lundqvist, and S. Lundqvist, *Solid State Commun.*, **9**, 537 (1971).

35. D. Bresser, E. Paillard, R. Kloepsch, S. Krueger, M. Fiedler, R. Schmitz, D. Baither, M. Winter, and S. Passerini, *Adv. Energy Mater.*, **3**, 513 (2013).
36. C. J. Cong, L. Liao, Q. Y. Liu, J. C. Li, and K. L. Zhang, *Nanotechnology*, **17**, 1520 (2006).
37. R. D. Shannon, *Acta Crystallogr., Sect. A*, **32**, 751 (1976).
38. C. Guglieri, E. Céspedes, C. Prieto, and J. Chaboy, *J. Phys. Condens. Matter*, **23**, 206006 (2011).
39. G. Giuli, A. Trapananti, F. Mueller, D. Bresser, F. Dácapito, and S. Passerini, *Inorg. Chem.*, **54**, 9393 (2015).
40. T. L. Phan, P. Zhang, D. S. Yang, N. X. Nghia, and S. C. Yu, *J. Appl. Phys.*, **110**, 063912 (2011).
41. B. Gilbert, B. H. Frazer, A. Belz, P. G. Conrad, K. H. Nealson, D. Haskel, J. C. Lang, G. Srajer, and G. De Stasio, *J. Phys. Chem. A*, **107**, 2839 (2003).
42. T. Yamamoto, *X-Ray Spectrom.*, **37**, 572 (2008).
43. M. Giorgetti, D. Wang, G. Aquilanti, D. Buchholz, and S. Passerini, *J. Phys. Conf. Ser.*, **712**, 012130 (2016).
44. H. Kim, D. H. Seo, H. Kim, I. Park, J. Hong, K. Y. Park, and K. Kang, *Chem. Mater.*, **24**, 720 (2012).
45. T. Eisenmann, J. Asenbauer, S. J. Rezvani, T. Diemant, R. J. Behm, D. Geiger, U. Kaiser, S. Passerini, and D. Bresser, *Small Methods*, 2001021 (2021).
46. J. Asenbauer, M. Kuenzel, T. Eisenmann, A. Birrozzi, J. Chang, S. Passerini, and D. Bresser, *J. Phys. Chem. Lett.*, **11**, 8238 (2020).
47. C. J. Pelliccione, Y. Ding, E. V. Timofeeva, and C. U. Segre, *J. Electrochem. Soc.*, **162**, A1935 (2015).
48. J. A. Oberteuffer and J. A. Ibers, *Acta Crystallogr. Sect. B Struct. Crystallogr. Cryst. Chem.*, **26**, 1499 (1970).
49. M. Giorgetti, S. Mukerjee, S. Passerini, J. McBreen, and W. H. Smyrl, *J. Electrochem. Soc.*, **148**, A768 (2001).
50. Z. Zhao, G. Tian, A. Sarapulova, G. Melinte, J. L. Gómez-Urbano, C. Li, S. Liu, E. Welter, M. Etter, and S. Dsoke, *ACS Appl. Mater. Interfaces*, **11**, 29888 (2019).
51. Y. Ma, U. Ulissi, D. Bresser, Y. Ma, Y. Ji, and S. Passerini, *Electrochim. Acta*, **258**, 535 (2017).